

First results from the search for an excess of $\bar{\nu}_e$ events in JSNS²

D. H. Lee,^{1,*} S. Ajimura,² A. Antonakis,³ M. Botran,³ M. K. Cheoun,⁴ J. H. Choi,⁵ J. W. Choi,⁶ J. Y. Choi,⁷ T. Dodo,^{8,9} H. Furuta,⁸ J. H. Goh,¹⁰ M. Harada,¹¹ S. Hasegawa,^{9,11} Y. Hino,^{8,†} T. Hiraiwa,^{2,‡} W. S. Hwang,¹⁰ T. Iida,¹² E. Iwai,^{3,‡} S. Iwata,^{13,§} H. I. Jang,⁷ J. S. Jang,¹⁴ M. C. Jang,⁶ H. K. Jeon,¹⁵ S. H. Jeon,⁵ K. K. Joo,⁶ D. E. Jung,⁶ S. K. Kang,¹⁶ Y. Kasugai,¹¹ T. Kawasaki,¹³ E. M. Kim,⁶ E. J. Kim,¹⁷ J. Y. Kim,⁶ S. Y. Kim,⁶ S. B. Kim,¹⁸ W. Kim,¹⁹ H. Kinoshita,¹¹ T. Konno,¹³ K. Kuwata,⁸ S. Lee,¹⁰ I. T. Lim,⁶ C. Little,³ T. Maruyama,¹ E. Marzec,³ S. Masuda,¹¹ S. Meigo,¹¹ S. Monjushiro,¹ D. H. Moon,⁶ T. Nakano,² M. Niiyama,²⁰ K. Nishikawa,^{1,¶} M. Noumachi,² M. Y. Pac,⁵ B. J. Park,¹⁹ H. W. Park,⁶ J. B. Park,⁴ Jisu Park,⁶ J. S. Park,¹⁹ R. G. Park,⁶ S. J. M. Peeters,²¹ G. Roellinghoff,¹⁵ C. Rott,²² J. W. Ryu,¹⁹ K. Sakai,¹¹ S. Sakamoto,¹¹ T. Shima,² C. D. Shin,⁵ J. Spitz,³ I. Stancu,²³ F. Suekane,⁸ Y. Sugaya,² K. Suzuya,¹¹ M. Taira,¹ Y. Takeuchi,¹² W. Wang,¹⁸ J. Waterfield,²¹ W. Wei,¹⁸ R. White,²¹ Y. Yamaguchi,¹¹ M. Yeh,²⁴ I. S. Yeo,⁵ C. Yoo,¹⁰ I. Yu,¹⁵ and A. Zohaib⁶

(JSNS² Collaboration)

¹High Energy Accelerator Research Organization (KEK), 1-1 Oho, Tsukuba, Ibaraki, 305-0801, Japan

²Research Center for Nuclear Physics, Osaka University,
10-1 Mihogaoka, Ibaraki, Osaka, 567-0047, Japan

³University of Michigan, 500 S. State Street, Ann Arbor, Michigan 48109, USA

⁴Department of Physics and OMEG Institute, Soongsil University,
369 Sangdo-ro, Dongjak-gu, Seoul, 06978, Korea

⁵Laboratory for High Energy Physics, Dongshin University,
67, Dongshindae-gil, Naju-si, Jeollanam-do, 58245, Korea

⁶Department of Physics, Chonnam National University,
77, Yongbong-ro, Buk-gu, Gwangju, 61186, Korea

⁷Department of Fire Safety, Seoyeong University, 1 Seogang-ro, Buk-gu, Gwangju, 61268, Korea

⁸Research Center for Neutrino Science, Tohoku University,
6-3 Azaaoba, Aramaki, Aoba-ku, Sendai, Miyagi 980-8578, Japan

⁹Advanced Science Research Center, JAEA, 2-4 Shirakata, Tokai-mura, Naka-gun, Ibaraki 319-1195, Japan

¹⁰Department of Physics, Kyung Hee University, 26,
Kyungheedae-ro, Dongdaemun-gu, Seoul 02447, Korea

¹¹J-PARC Center, JAEA, 2-4 Shirakata, Tokai-mura, Naka-gun, Ibaraki 319-1195, Japan

¹²Faculty of Pure and Applied Sciences, University of Tsukuba,
Tennodai 1-1-1, Tsukuba, Ibaraki, 305-8571, Japan

¹³Department of Physics, Kitasato University, 1 Chome-15-1 Kitazato,
Minami Ward, Sagamihara, Kanagawa, 252-0329, Japan

¹⁴GIST College, Gwangju Institute of Science and Technology,
123 Cheomdangwagi-ro, Buk-gu, Gwangju, 61005, Korea

¹⁵Department of Physics, Sungkyunkwan University, 2066,
Seobu-ro, Jangan-gu, Suwon-si, Gyeonggi-do, 16419, Korea

¹⁶School of Liberal Arts, Seoul National University of Science and Technology,
232 Gongneung-ro, Nowon-gu, Seoul, 139-743, Korea

¹⁷Division of Science Education, Jeonbuk National University,
567 Baekje-daero, Deokjin-gu, Jeonju-si, Jeollabuk-do, 54896, Korea

¹⁸School of Physics, Sun Yat-sen (Zhongshan) University, Haizhu District, Guangzhou, 510275, China

¹⁹Department of Physics, Kyungpook National University, 80 Daehak-ro, Buk-gu, Daegu, 41566, Korea

²⁰Department of Physics, Kyoto Sangyo University,
Motoyama, Kamigamo, Kita-Ku, Kyoto-City, 603-8555, Japan

²¹Department of Physics and Astronomy, University of Sussex, Falmer, Brighton, BN1 9RH, United Kingdom

²²Department of Physics and Astronomy, University of Utah,
201 Presidents' Cir, Salt Lake City, UT 84112, U.S.A

²³University of Alabama, Tuscaloosa, AL, 35487, USA

²⁴Brookhaven National Laboratory, Upton, NY 11973-5000, U.S.A.

(Dated: February 9, 2026)

The JSNS² (J-PARC Sterile Neutrino Search at the J-PARC Spallation Neutron Source) experiment at the Material and Life Science Facility (MLF) of J-PARC is designed to directly test an excess on $\bar{\nu}_e$ events which was indicated by LSND (Liquid Scintillator Neutrino Detector). The combination of a short-pulsed proton beam and a gadolinium-loaded liquid scintillator provides an excellent signal-to-noise ratio. In this article, we report the first results of a direct test based on data collected in 2022. After applying all event selection criteria, two events are observed, consistent with the expected background of 2.3 ± 0.4 events. No excess of $\bar{\nu}_e$ events are seen in this report, however the expected number of events due to LSND anomaly is 1.1 ± 0.5 , thus this result is not yet

conclusive. Data taking has been ongoing since 2021 and will continue in future runs. In addition, a new far detector has recently been constructed for the second phase experiment, JSNS²-II, marking an important milestone toward forthcoming measurements.

I. INTRODUCTION

JSNS² [1, 2] aims to directly test an excess of $\bar{\nu}_e$ events which was indicated by LSND [3], the so called LSND anomaly. LSND reported a significant excess of observed $\bar{\nu}_e$ events above background with the neutrinos produced by muon decay-at-rest and the liquid scintillator detector, thus JSNS² employs a same neutrino source, target, and detection principle as LSND, while incorporating modern technologies such as Gd-loaded liquid scintillator (Gd-LS), 500 MHz flash ADCs (FADCs), and a short pulsed proton beam to perform a stringent test. This excess may be related to observations reported by other experiments [4–6], such as the sterile neutrino hypothesis that induces short-baseline neutrino oscillations; the results from JSNS² will also provide further insight into these interpretations.

The JSNS² experiment employs a 50-ton liquid scintillator detector on the third floor of the MLF, at a baseline of 24 m from the neutrino source [7]. The neutrino source is a liquid-mercury target designed to withstand a 1 MW proton beam. Although originally constructed as a spallation neutron source for material and life science studies, the mercury target simultaneously produces (anti)neutrinos. JSNS² utilizes (anti)neutrinos from muon decay at rest ($\mu^+ \rightarrow e^+ + \nu_e + \bar{\nu}_\mu$) to test the anomaly. Protons are accelerated to 3 GeV by the Rapid Cycling Synchrotron at J-PARC and impinge on the mercury target. The beam operates at 25 Hz with two 100 ns wide bunches separated by 600 ns, providing excellent temporal separation between the signal and backgrounds. The designed 1 MW beam power was achieved in 2024. Using the $^{12}\text{C}(\nu_e, e^-)^{12}\text{N}_{g.s.}$ reaction (CNgs), the number of positive muons produced per proton at the target is measured to be 0.48 ± 0.17 [8], which is about an order of magnitude larger than that of the KARMEN experiment [9] owing to the MLF’s higher proton beam energy. The $\bar{\nu}_e$ signal is detected through the inverse beta decay (IBD) reaction, $\bar{\nu}_e + p \rightarrow e^+ + n$, in the liquid scintillator. The neutrino target scintillator contains 0.1% Gd by mass, enabling enhanced neutron capture after thermalization, which results in a \sim 8 MeV γ -rays cascade after a mean capture time of \sim 30 μs . The prompt signal from the positron and the delayed signal from Gd capture form a coincidence signal-

ture. The most severe background arises from cosmogenic neutrons, which can mimic this coincidence by their recoil protons and captured neutrons [10]. To suppress such backgrounds, 10% di-isopropyl naphthalene (DIN, $\text{C}_{16}\text{H}_{20}$) was dissolved into the Gd-LS from 2021 to 2022. DIN enhances pulse-shape discrimination (PSD) performance for prompt candidates. A dedicated PSD algorithm utilizing full waveform information and a log-likelihood ratio method was developed to further reduce neutron-induced backgrounds [11].

Commissioning data were collected in 2020 [10], and physics data have been accumulated since 2021. Despite annual installation and dismantling of the detector and scintillator at MLF, no significant degradation of the scintillator performance has been observed. In total, JSNS² accumulated 5.14×10^{22} protons on target (POT) from 2021 to 2025. This article reports results from the 2022 dataset (0.82×10^{22} POT), corresponding to the first period with 10% DIN concentration in the Gd-LS.

II. JSNS² DETECTOR

Reference [7] provides a detailed description of the JSNS² detector; only the components relevant to this report are summarized here.

The cylindrical detector consists of three concentric layers of liquid scintillator. From the innermost to the outermost regions the three concentric layers are the inner target, then the surrounding gamma-catcher and the veto layer. The inner target is filled with Gd-loaded liquid scintillator (Gd-LS) with 10% DIN, and both gamma-catcher and veto layers contain pure liquid scintillator (pure LS) which have neither Gd nor DIN. The target region is contained in an acrylic vessel with a diameter of 3.2 m and a height of 2.5 m. The gamma-catcher and veto layers each have a typical thickness of 25 cm and are optically separated by black acrylic plates. All layers are housed within a stainless-steel tank with a diameter of 4.6 m and a height of 3.5 m [12]. The target contains approximately 17 tons of Gd-LS, while the outer regions together hold about 33 tons of pure LS. The base solvent of both Gd-LS and pure LS is linear alkylbenzene (LAB), containing 3 g/L of 2,5-diphenyloxazole (PPO) as the primary fluor, and 15 mg/L (Gd-LS) and 30 mg/L (pureLS) of 1,4-bis(2-methylstyryl)benzene (bis-MSB) as a secondary wavelength shifter. DIN (produced by Eljen company: EJ-309 [13]) exhibits long-term stability suitable for extended physics runs owing to its high chemical purity. Particles with large energy loss per unit length (dE/dx), in particular in DIN-containing scintillator, produce scintillation light with broader timing profiles and longer decay tails than those with small dE/dx particles. The typical PSD perfor-

* leedh@post.kek.jp

† Now at KEK

‡ Now at RIKEN

§ Now at Tokyo Metropolitan College of Industrial Technology (Tokyo Metro. Col. of Indus. Tech.)

¶ Deceased

mance of the JSNS² detector is described in Ref. [11]. Using DIN and a dedicated likelihood-based PSD algorithm, the experiment achieved a neutron rejection efficiency of $95.0 \pm 0.2\%$ while maintaining a Michel-electron identification efficiency of $92.8 \pm 1.8\%$. To reconstruct events in the target and gamma-catcher regions from scintillation light, ninety-six 10-inch Hamamatsu R7081 photomultiplier tubes (PMTs) are installed around the boundary between the gamma-catcher and veto layers. An additional twenty-four PMTs are mounted in the veto region to detect incoming particles such as cosmic-ray muons entering the detector.

Signals from all 120 PMTs are digitized using 500 MHz, 8-bit FADCs [14]. A coincidence trigger has been implemented to efficiently acquire both prompt and delayed signals from IBD events. A prompt trigger is issued when the analog sum of the 96 PMT signals from the target and gamma-catcher regions exceeds a threshold of approximately 200 mV (~ 5 MeV) within a $1.7\text{--}10\ \mu\text{s}$ window after the beam start timing. If a prompt trigger exists, a delayed trigger is generated when the analog sum exceeds about 70 mV (~ 2 MeV) within a time window of 25 ms after the prompt trigger. The beam timing in our trigger system is defined by a signal sent directly from the radio-frequency module of J-PARC accelerator.

III. CALIBRATIONS

In selecting IBD candidates, the event energy and vertex are reconstructed using the JADE (JSNS² Analysis Development Environment) software framework [15], which employs a likelihood maximization algorithm. Detector calibrations to validate JADE were carried out with one- and three-dimensional calibration systems using ^{252}Cf sources providing a cascade of γ -rays totaling ~ 8 MeV from neutron captures on Gd (n-Gd) and with cosmogenic Michel-electrons, whose endpoint energy is ~ 53 MeV [16]. JSNS² adopts a simple charge-prediction model for the PMTs, parameterized by the distance and zenith angle between the scintillation light source and the center of each PMT sphere, which provides reliable event reconstruction performance.

After calibration, the reconstructed energy scale varies by a few percent over time and across vertex positions. These variations are corrected using cosmogenic Michel-electrons and n-Gd capture events observed in physics data made by cosmogenic neutrons, and are properly accounted for this analysis. The typical energy calibration using Michel-electrons is also shown in Ref. [17]. The systematic uncertainty on the energy scale after calibration is estimated to be 0.8%. The uncertainty on the fiducial volume, determined from the three-dimensional ^{252}Cf calibration, is currently $\sim 20\%$ [16].

IV. EVENT SELECTION

The event selection is optimized to efficiently search for an excess of $\bar{\nu}_e$ IBD events. Table I summarizes IBD event selection criteria, and their efficiencies and uncertainties, evaluated to detect $\bar{\nu}_e$ IBD events. The fiducial volume for this analysis is specified as $r < 140$ cm and $|z| < 100$ cm, where the origin is set at the center of the target ($r = \sqrt{x^2 + y^2}$). Further details are provided in the following.

TABLE I. IBD selection criteria, and their efficiencies and uncertainties evaluated for the LSND anomaly are summarized. The efficiencies are determined using a combination of data and Monte Carlo simulation. Each efficiency is quote relative to the previous efficiencies, and the cumulative total is given at the end.

Requirement	Relative Efficiency (%)
–Prompt Candidate–	
$20 \leq E_p \leq 60$ MeV	100.0
$2 \leq \Delta T_{beam-p} \leq 10\ \mu\text{s}$	46.5 ± 0.5
PSD	87.2 ± 9.1
–Delayed Candidate–	
$7 \leq E_d \leq 12$ MeV	75.3 ± 0.9
Beam neutron rejection	94.1 ± 0.1
–IBD paired Candidate–	
$\Delta T_{p-d} \leq 100\ \mu\text{s}$	$96.6^{+3.4}_{-5.6}$
$\Delta VTX_{p-d} \leq 60$ cm	83.4 ± 10.0
Background rejection likelihood	70.5 ± 1.5
–Muon and Michel electron rejections–	
Muon rejection	92.8 ± 0.5
Michel electron rejections (veto layer)	97.0 ± 0.03
Michel electron rejections (baseline)	86.1 ± 1.4
Chimney passing muon rejections	98.7 ± 0.1
Cumulative total efficiency	$12.4^{+2.1}_{-2.2}$

A. IBD Prompt Candidates

The IBD prompt-energy selection is identical to that of LSND to have a model-independent test. The selection efficiency, $20 \leq E_p \leq 60$ MeV, including the detector's trigger efficiency, is 100%. However, under a sterile neutrino hypothesis, the energy selection's efficiency is sensitive to oscillation parameters, thus this dependency is described and consider further later.

The timing of the IBD prompt candidates relative to the beam pulse, ΔT_{beam-p} , is required to satisfy $2 \leq \Delta T_{beam-p} \leq 10\ \mu\text{s}$. When the proton beam with two bunches impinges on the mercury target, muons are produced with a lifetime of $2.2\ \mu\text{s}$. Consequently, the expected arrival time of the $\bar{\nu}_e$ events in the JSNS² detector with respect to the beam start is shown in Fig. 1(a). This $8\ \mu\text{s}$ time window strongly suppresses the cosmogenic backgrounds. In addition, events with $\Delta T_{beam-p} \leq 2\ \mu\text{s}$

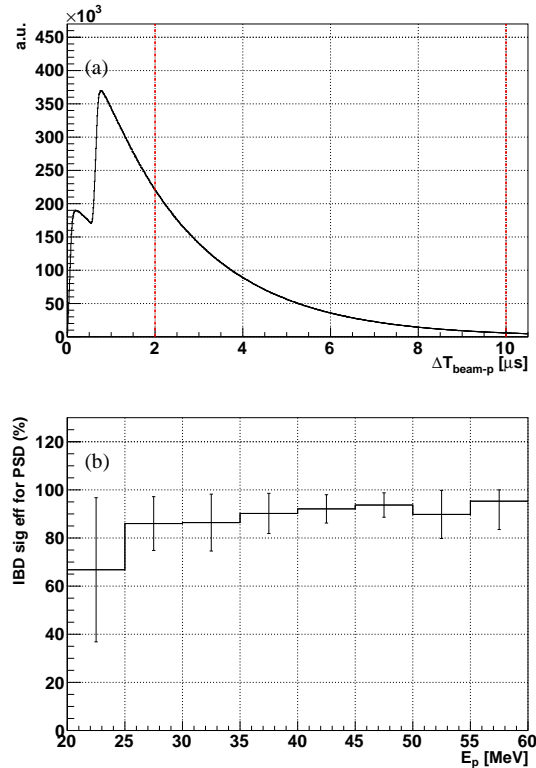


FIG. 1. (a) Expected timing distribution of IBD prompt candidates relative to the beam start, obtained from MC simulation. (b) PSD selection efficiency for IBD events as a function of energy. The vertical axes of (a) is in arbitrary units.

are rejected to suppress backgrounds from beam neutrons and neutrinos produced by π or K decays. The clocks of FADCs are synchronized with the 40 ms accelerator repetition cycle, and the uncertainty associated with the FADC timing is negligible. The dominant systematic uncertainty for this selection arises from the trigger dead-time stability, estimated to be approximately 1%.

The PSD capability was originally evaluated using cosmogenic Michel-electrons as a control sample [11]. However, subsequent studies revealed baseline shifts in the FADC readout following muon events due to electronics effects [18], rendering Michel-electrons unsuitable for PSD evaluation in IBD analyses. Instead, a γ -ray control sample is used to determine the PSD performance. Figure 1(b) shows the updated PSD efficiency as a function of energy while requiring approximately 99.7% rejection of cosmogenic neutrons used in this manuscript. Uncertainties are derived from differences between the methods used to evaluate this efficiency.

B. IBD Delayed Candidates

The delayed IBD candidates originate from neutron captures on Gd, releasing gamma rays with a total energy of approximately 8 MeV. Figure 2(a) shows the

reconstructed energy spectra of simulated and observed n-Gd capture events, denoted as E_d . The observed distribution is obtained from cosmogenic neutron samples, and good agreement is found between data and MC using this control sample. A delayed-energy selection of $7 \leq E_d \leq 12$ MeV is applied to identify IBD candidates. The uncertainty in the delayed energy selection efficiency includes contributions from both the energy scale uncertainty and the n-Gd capture efficiency. Since the JSNS² Gd-LS was donated by the Daya Bay experiment, the latter uncertainty value follows that reported in Ref. [19].

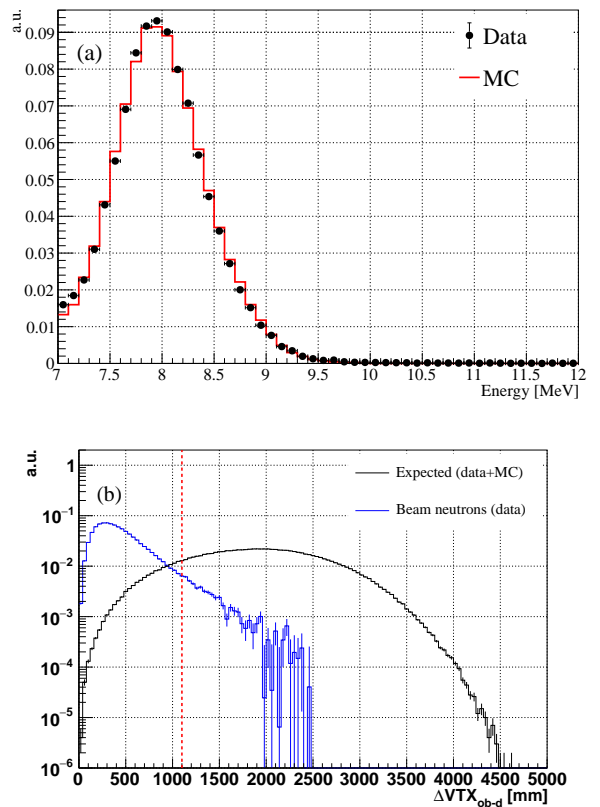


FIG. 2. (a) Expected and observed reconstructed energy spectra of IBD delayed candidates. (b) Expected ΔVTX_{OB-d} distribution (black: data + MC) and that from beam neutrons (blue: data). The red line indicates the applied selection threshold. All plots are area normalized.

Beam-related neutron backgrounds can be suppressed using the prompt timing variable, ΔT_{beam-p} , by selecting prompt candidates with higher energy due to the shorter time-of-flight from the mercury target to the detector. However, neutrons that are thermalized within the target region can produce delayed background candidates. To reject such events, JSNS² developed a spatial correlation rejection. If an activity that occurred during the beam time window ("OB" timing) is spatially close to an n-Gd capture vertex ("d" vertex), the event is identified as originating from a beam neutron. Thus, we

required $\Delta VTX_{OB-d} \geq 110$ cm, where ΔVTX_{OB-d} is the spatial distance between them. Figure 2(b) shows the expected ΔVTX_{OB-d} distributions for IBD events (black, data+MC) and beam-neutron backgrounds (blue, data). The red line indicates the applied selection threshold. The IBD selection efficiency for this criterion is $94.1 \pm 0.1\%$. The event multiplicity during the beam time window is also taken into account; in cases with no beam-related activity, about half of beam spills, no rejections on ΔVTX_{OB-d} are applied, resulting in the signal selection efficiency is effectively 100%. The dominant systematic uncertainty arises from the vertex reconstruction accuracy, as discussed in Ref. [16]. The overall beam-neutron rejection efficiency achieved by this selection is approximately 93%.

C. IBD paired candidates

The timing and spatial correlations between the IBD prompt and delayed candidates provide powerful discrimination between signal and background events. Neutron captures on Gd in Gd-LS occurs with a mean time of approximately $30 \mu\text{s}$; therefore, events are required to satisfy $\Delta T_{p-d} < 100 \mu\text{s}$. Figure 3 shows the ΔT_{p-d} distributions for IBD events (MC: black) and cosmogenic neutron samples obtained from data (red) and MC (orange). Since no IBD data sample is available to directly assess the systematic uncertainty, the difference between data and MC for the cosmogenic neutron sample is used to estimate it, assuming similar behavior between neutron and IBD events. The efficiency derived from the IBD MC is $96.6^{+3.4\%}_{-5.6\%}$.

Applying the same approach to the spatial correlation selection, ΔVTX_{p-d} , yields an efficiency of $83.4 \pm 10.0\%$. The distributions for the IBD MC, the cosmogenic neutron background data and the accidental background are shown in Fig. 3(b).

Signal and background discrimination is further enhanced by a likelihood ratio constructed from six variables: ΔT_{beam-p} , E_d , ΔT_{p-d} , ΔVTX_{p-d} , and the reconstructed vertex coordinates y (beam direction) and z (vertical direction). This multivariate likelihood selection depends sensitively on the background modeling, which is discussed in detail in a later section.

D. Rejection of cosmic rays

JSNS² is an above-ground experiment, with its detector located on the third floor of the MLF building. Consequently, suppression of cosmogenic backgrounds is essential. The detector's veto region and additional techniques are fully utilized for this purpose.

For the muon veto, the summed charge of the twelve PMTs in the top veto region is required to be less than 30 photoelectrons (p.e.), and that of the twelve PMTs

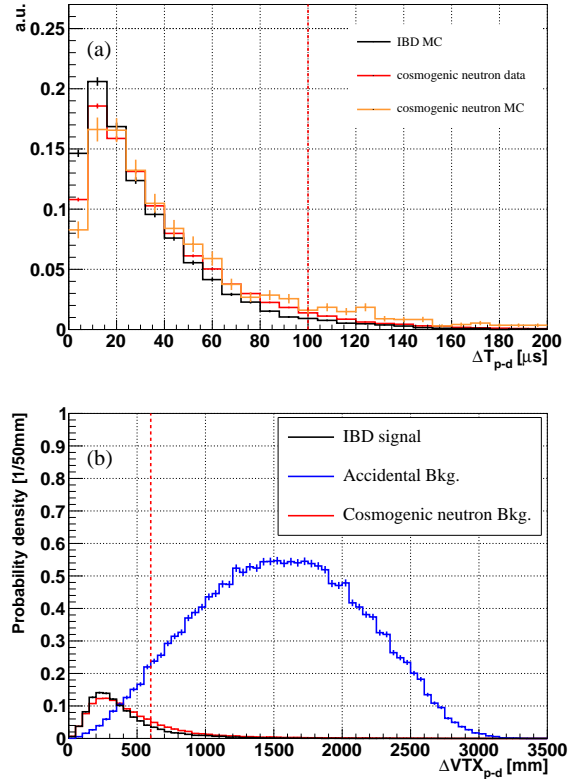


FIG. 3. (a) ΔT_{p-d} distributions for the IBD (MC: black), cosmogenic neutron samples from data (red) and MC (orange). The plot is area normalized. (b) ΔVTX_{p-d} . Black corresponds to the IBD signal, blue shows the accidental background and red shows the cosmogenic neutrons. For (b), all distributions are area normalized to one after applying the $\Delta VTX_{p-d} < 60$ cm selection.

in the bottom region less than 40 p.e., within a 200 ns time window relative to the activity in the target volume. This requirement is applied to both prompt and delayed candidates. The inefficiency of this veto for IBD signals is evaluated using cosmogenic control samples: Michel-electrons for prompt candidates and gammas from n-Gd captures for delayed candidates. The resulting IBD selection efficiency from this veto is $92.8 \pm 0.5\%$. After the muon veto, cosmogenic Michel-electrons remain as a dominant background, particularly for prompt candidates. To reject them, parent muons are searched for within $10 \mu\text{s}$ before the target activity (“Michel-e veto”). The criterion for identifying a parent muon is a summed charge exceeding 100 p.e. in either the top or bottom twelve PMTs. With a muon rate of approximately 2 kHz, the accidental-coincidence probability between a muon and an IBD event occurring within the $10 \mu\text{s}$ search window in the IBD delayed region is about 2%. Considering a trigger dead time for the IBD prompt candidates, the inefficiency of the Michel-electron veto is about 0.9%, corresponding to a signal selection efficiency of $97.0 \pm 0.03\%$ in total.

Due to the trigger dead time, some Michel-electrons still contaminate the IBD prompt candidate sample. To remove these, JSNS² developed an innovative method to tag muons and Michel-electrons using the FADC baseline [18]. High-energy particles cause a measurable shift in the FADC baseline following their passage. This feature allows us to tag Michel-electrons with their hidden parent muons with 99.8% efficiency. However, this method introduces a small probability for real IBD events to be incorrectly rejected due to a large charge event preceding it. High-energy beam neutrons during the beam window can also induce baseline shifts, resulting in the additional inefficiency. Accounting for these effects, the IBD selection efficiency on this baseline cut is $86.1 \pm 1.4\%$.

The central chimney structure of the detector provides necessary access to the inner volume, but lacks veto coverage. If a muon traverses this region and produces an event within the 20–60 MeV energy range, neither the veto nor the FADC baseline method can identify it. Because scintillation light is hidden by the chimney structure, the reconstructed vertex shows poor fit quality [11]. This “goodness” parameter is used to reject such background events. The corresponding IBD selection efficiency with this criterion is $98.7 \pm 0.1\%$.

The dominant systematic uncertainty for the cosmic-ray veto arises from detector stability. The uncertainty for the Michel-electron rejection using the FADC-baseline shift includes the difference observed between a sideband-region sample (described later) and a single-triggered control sample.

V. BACKGROUNDS

Two main background sources are considered in this analysis: accidental coincidences and cosmogenic neutrons.

The accidental background is described in detail in Ref. [20]. The rate of accidentals backgrounds passing the IBD prompt selection in Table I is $[(8.5 \pm 0.1) \times 10^{-5}/\text{beam spill}]$, which is dominated by cosmogenic γ -rays. The corresponding rate for accidentals passing the IBD delayed selection is $[(1.9 \pm 0.01) \times 10^{-2}/\text{beam spill}]$. The primary contributions to this background are (a) residual beam neutrons ($\sim 50\%$), (b) beam-induced γ rays ($\sim 25\%$), and (c) cosmogenic γ -rays. To suppress accidental coincidences, a spatial correlation requirement of $\Delta\text{VTX}_{p-d} < 60$ cm is applied, which plays a crucial role in reducing uncorrelated events. Using a dedicated calibration run with beam-scheduled timing triggers and the spill-shift method [20], the rejection factor for accidental backgrounds is found to be approximately 94.7% (Fig. 3(b)).

Neutrons constitute a correlated background, fully mimicking the IBD signature and therefore not removed by the standard IBD selections. Their rejection relies primarily on (a) PSD and (b) a likelihood-ratio discrimination method. The cosmogenic neutron control sample

is defined by events occurring later than 1 ms after the beam start. PSD application reduces this background by a factor of ~ 300 , and the likelihood-ratio provides an additional suppression by a factor of a few as described later.

The event rates and variable distributions for both accidental and correlated backgrounds are evaluated using in situ, data-driven control samples, not MC simulation. These samples include the correct background rejection factors a priori, and minimize systematic uncertainties associated with modeling, energy calibration, and time-dependent effects.

In addition to the backgrounds discussed above, a small contribution arises from neutrino-induced processes. The CNgs reaction produces background events when the subsequent β decay of $^{12}\text{N}_{g.s.}$ occurs within 100 μs . The in-situ measurements reported in Ref. [8] enable a data-driven estimation of this background. The beam intrinsic $\bar{\nu}_e$ component from the $\pi^- - \mu^-$ decay chain at the mercury target is evaluated solely by MC simulation, since the π^- production rate from 3 GeV proton interactions with mercury has not been directly measured. The uncertainty on this background is conservatively assigned as 50%, derived from the discrepancy between the measured and simulated CNgs rate from the $\pi^+ - \mu^+$ chain. Since these neutrino-induced backgrounds become relevant only after suppression of the dominant cosmogenic-neutron and accidental backgrounds, the corresponding rejection methods applied after the selections listed in Table I for the dominant ones are described in this section.

A. Multivariate Likelihood-ratio Selection

After applying the event selection summarized in Table I, several variables exhibit distinct differences between the IBD signal and background samples. Although these variables are not directly used for binary selection cuts, they provide significant discriminating power for the multivariate likelihood-ratio analysis.

Six input variables are used to construct the likelihood ratio: (a) ΔT_{beam-p} , (b) ΔT_{p-d} , (c) ΔVTX_{p-d} , (d) E_d , and the reconstructed vertices on (e) y (beam direction) and (f) z (vertical) coordinates. Cosmogenic backgrounds yield flat timing distributions in (a) and (b), but are concentrated at higher z , as expected for cosmic rays. In contrast, IBD events follow exponential timing and a flat z distribution. The accidental background shows no spatial correlation between prompt and delayed candidates, resulting in the uniform phase-space pattern visible in (c). For variables (b), (c), (e), (f), MC simulations are used to model the IBD signal, while for (a), corrected timing information from another neutrino source [17] is employed. Discrimination between accidental and IBD events is primarily achieved using all six variables, whereas separation between neutron-induced and IBD events relies mainly on (a) and (e). Probability

density functions (PDFs) for each component are constructed from these six variables. To ensure statistical independence, half of the background control sample is used to build the PDFs, while the remaining half is reserved for evaluating the likelihood-ratio scores.

A two-dimensional likelihood-ratio function is constructed to separate the signal from backgrounds: $LLK_{signal} - LLK_{accidental}$ and $LLK_{signal} - LLK_{neutron}$. LLK denotes the negative log-likelihood, and subscripts indicate the type of sample. In this analysis, the signal region of the two-dimensional log-likelihood ratio is defined as the area where both log-likelihood scores satisfy ≤ 0 .

The likelihood separation efficiency for IBD events is obtained as $70.5 \pm 1.5\%$. This method suppresses approximately 70% of neutron-induced backgrounds and 84% of accidental backgrounds. The dominant systematic uncertainty arises from the modeling of the IBD MC.

B. Energy Side-band Study

To validate the analysis methodology prior to extracting the search results, we performed an energy side-band study. Relative to the signal region defined in Table I, which applies $20 \leq E_p \leq 60$ MeV and $7 \leq E_d \leq 12$ MeV, four independent side-band regions were defined as follows: (A) E_{du} : delayed energy 12–20 MeV, (B) E_{dl} : 5–7 MeV, (C) E_{pu} : prompt energy 60–100 MeV, and (D) E_{pl} : 12–20 MeV, where the subscripts “*u*” and “*l*” denote “upper” and “lower” energy regions, respectively. All other selection criteria listed in Table I were applied unchanged, except for the E_{pl} region, where the lower bound of ΔT_{beam-p} was increased from 2 to 3 μ s to suppress beam-neutron contamination.

In these side-band regions, the expected selection efficiency for IBD events associated with the LSND anomaly, as well as for other neutrino-induced backgrounds, is at least an order of magnitude smaller than in the nominal selection. These contributions are therefore assumed to be negligible in the predicted event counts.

The number of selected events and the distributions of relevant variables were compared between data and prediction in four cases: (1) without pulse-shape discrimination (PSD) or log-likelihood ratio (LLK), (2) with LLK only, (3) with PSD only, and (4) with both PSD and LLK applied. The PSD threshold was set to reject more than 99.5% of neutron backgrounds, and the LLK criterion required both likelihood scores to be less than zero (i.e., signal-like events). Table II summarizes the observed and predicted event counts in each side-band region and for each case. Predictions include systematic uncertainties but not statistical (Poisson) uncertainties. For the E_{du} region, only case (1) is reported due to the limited number of events.

The predictions, composed of accidental and cosmogenic neutron background components estimated from data-driven control samples, are in good agreement with

the observations across all regions and selection stages. The shapes of the observed and predicted distributions for all variables also show a consistent behavior, validating the analysis procedure before applying it to the signal region.

VI. EXPECTED NUMBER OF SIGNAL EVENTS

The expected number of events associated with the LSND anomaly in JSNS² is described in this section. Two different estimation methods are described: a model-independent method based on LSND’s anomaly, and a method that assumes the excess is from short-baseline neutrino oscillations.

A. Normalization-based calculation

The normalization-based prediction employs Eq. 1,

$$N_{JSNS^2} = \frac{\Phi_{JSNS^2} \cdot \sigma \cdot N_T \cdot \epsilon_{JSNS^2}}{\Phi_{LSND} \cdot \sigma \cdot N_T \cdot \epsilon_{LSND}} \times N_{LSND}, \quad (1)$$

where Φ denotes the time-integrated neutrino flux at the detector in units of neutrinos per cm^2 , σ is the IBD cross section, N_T is the number of hydrogen atoms serving as antineutrino targets, ϵ is the event selection efficiency, and N is the number of events. We assume that the energy spectrum of $\bar{\nu}_e$ is identical for LSND and JSNS² in this calculation. Under this assumption, the neutrino flux scales with the inverse square of the baseline, while the IBD cross section is common to both experiments and cancels out.

Table III summarizes the parameters used in Eq. 1 for LSND [3] and JSNS². The quantity $\#\mu/\text{p}$ represents the number of positive muons produced per incident proton at the neutrino production target, and N_{eve} is the observed number of events in LSND, and the expected number of events from the LSND anomaly with this normalization for JSNS². In the present analysis, JSNS² benefits from a higher antineutrino flux per proton due to the higher proton beam energy, whereas LSND achieved a larger effective target mass and higher detection efficiency.

The excess of $\bar{\nu}_e$ events observed by LSND is 87.9 ± 22.4 (stat) ± 6.0 (syst). Using Eq. 1, this corresponds to an expected number of 1.1 ± 0.5 LSND anomaly events in JSNS². The uncertainty is dominated by the muon production measurement in JSNS², which is limited by statistics and fiducial volume definition, as well as by the uncertainty of the LSND measurement itself.

For reference, Table III also includes the corresponding parameters for the KARMEN experiment [9], which also directly tested the LSND anomaly. KARMEN observed 15 events, compared with an expectation of 28.4 ± 6.3

TABLE II. Comparison of the number of events between the observations and the predictions for each side-band region and each analysis step. The predictions include only systematic uncertainties.

cases	E_{du} obs.	pred.	E_{dl} obs.	pred.	E_{pu} obs.	pred.	E_{pl} obs.	pred.
w/o PSD w/o LLK	3	3.5 ± 0.7	91	106.3 ± 2.7	703	711.7 ± 16	191	184.6 ± 5.2
w/o PSD w/ LLK	–	–	25	27.4 ± 0.8	240	213.6 ± 4.8	49	50 ± 1.5
w/ PSD w/o LLK	–	–	2	5.1 ± 0.3	5	5.4 ± 0.3	6	3.3 ± 0.2
w/ PSD w/ LLK	–	–	0	0.9 ± 0.1	1	1.2 ± 0.2	0	0.5 ± 0.08

TABLE III. A comparison between LSND, KARMEN and JSNS² on a neutrino flux (number of neutrinos per cm^2), a number of targets for anti electron neutrinos (N_T), the selection efficiency (%). The observed number of events in LSND, and the expected number of events for JSNS² and KARMEN from the LSND anomaly are also shown (N_{eve}).

item	LSND	KARMEN	JSNS ²
ν flux ($\#\nu/\text{cm}^2$)	1.26×10^{14}	6.89×10^{13}	5.47×10^{13}
(POT)	1.81×10^{23}	6.05×10^{22}	0.82×10^{22}
(# μ/p)	0.079	0.0448 ± 0.0030	0.48 ± 0.17
(baseline)	30 m	17.7 m	24 m)
N_T	7.4×10^{30}	4.5×10^{30}	7.48×10^{29}
efficiency (%)	42.0 ± 3.0	19.1 ± 1.45	$12.5_{-2.2}^{+2.1}$
N_{eve}	87.9 ± 23.1	12.6 ± 3.3	1.1 ± 0.5

events under the LSND-anomaly hypothesis (including backgrounds), corresponding to a 2.1σ tension. In this context, JSNS² plays an essential role in clarifying the tension between the LSND and KARMEN results.

B. Oscillation-based calculation

Beyond the normalization-based discussion above, neutrino oscillation effects at short baselines can also be considered separately. In this case, the oscillated $\bar{\nu}_e$ originates from $\bar{\nu}_\mu$ produced in the reaction $\mu^+ \rightarrow e^+ + \nu_e + \bar{\nu}_\mu$ in the mercury target. The energy spectrum ranges from 0 to 52.8 MeV, and is weighted by an oscillation probability. We assume two-flavor neutrino oscillations between $\bar{\nu}_\mu$ and $\bar{\nu}_e$, expressed as

$$P(\bar{\nu}_\mu \rightarrow \bar{\nu}_e) = \sin^2(2\theta_{\mu e}) \cdot \sin^2\left(\frac{1.27\Delta m^2 L}{E_{\bar{\nu}}}\right), \quad (2)$$

where P is the oscillation probability, $\theta_{\mu e}$ is the mixing angle between muon and electron antineutrinos, Δm^2 (eV²) is the squared mass difference between the two mass eigenstates, $E_{\bar{\nu}}$ is the antineutrino energy (MeV), and L is the distance between the neutrino production and detection points (meter).

The IBD cross section is known with high precision (e.g.: [21]). The IBD reaction produces a positron with a kinetic energy of $(E_{\bar{\nu}_e} - 1.8)$ MeV approximately, which constitutes the prompt signal. Including the contribution

from positron annihilation, the visible (deposited) energy in the detector is approximately $E_{\text{vis}} \simeq T_{e^+} + 2m_e$, and the reconstructed prompt energy E_p is derived from this visible energy.

Assuming the LSND best-fit oscillation parameters, $(\sin^2 2\theta, \Delta m^2) = (0.003, 1.2)$, reported in Ref. [3], the expected number of events in JSNS² is 1.2 ± 0.4 .

VII. RESULTS

Table IV summarizes the observed and predicted numbers of events in the IBD signal region defined in Table I for each analysis case, which has the same definition as those in side-bands. The predictions assume no LSND anomaly contribution, while including the intrinsic $\bar{\nu}_e$ and the CNgs backgrounds. A total of 2 events are observed, consistent with the background-only expectation of 2.3 ± 0.4 events. No clear excess of $\bar{\nu}_e$ events is seen with the present statistics. The expected number of $\bar{\nu}_e$ events due to LSND anomaly defined by the normalization-base calculation is 1.1 ± 0.5 as mentioned above.

After applying both PSD and LLK selections, the predicted background composition consists of cosmogenic neutrons (0.6 ± 0.2 events), accidental coincidences (1.00 ± 0.01), CNgs (0.08 ± 0.02) and intrinsic beam-related backgrounds (0.6 ± 0.3).

Figure 4 shows the PSD score distribution after applying all selection criteria except for the PSD cut, while Fig. 5 presents the distributions of reconstructed timing and vertex after the PSD selection. The applied PSD score threshold ranges from 550 to 730 depending on energy. The observed distributions agree well with the expected ones across all variables, confirming the consistency of the event selection and background modeling. Figure 6 gives the 2D LLK distributions for the observations overlaid with the backgrounds, which have a good agreement. The LLK selection requires both the horizontal and vertical log-likelihood scores to be less than zero, corresponding to the signal-like region.

A. Neutrino oscillation interpretation

These results can also be interpreted to the neutrino oscillation hypothesis. The 90% confidence level (C.L.) exclusion region derived from this analysis is shown in Fig. 7.

TABLE IV. Comparison of the number of events between the observation and the prediction for the signal-region in each analysis step. The predictions include only systematic uncertainties.

cases	observation	prediction
w/o PSD w/o LLK	1079	1063.0 ± 25.7
w/o PSD w/ LLK	304	315.8 ± 8.0
w/ PSD w/o LLK	10	11.2 ± 0.7
w/ PSD w/ LLK	2	2.3 ± 0.4

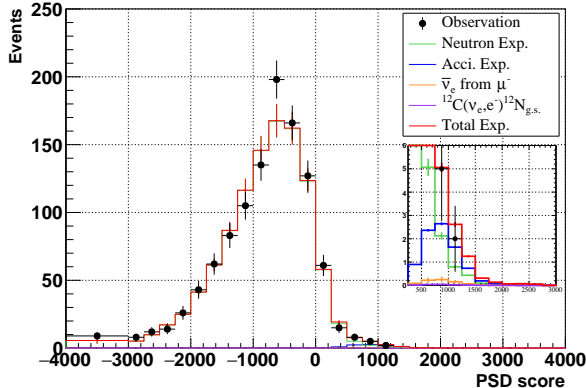


FIG. 4. PSD score distribution after applying the selection criteria listed in Table I. The inset shows an expanded view of the same distribution. The vertical axis indicates the number of events.

Feldman–Cousins statistics [22] are employed, incorporating fluctuations of the expected background and signal yields using Poisson statistics, with systematic uncertainties included at each ($\sin^2 2\theta$, Δm^2) point. The 90% and 99% C.L. allowed regions from the LSND experiment are also shown for comparison. The energy dependence of efficiencies on the IBD prompt energy and PSD are taken into account in constructing the exclusion curve.

VIII. SUMMARY

We report the first results from a direct tests of LSND anomaly regarding the excess of $\bar{\nu}_e$ events in JSNS² using 2022 data. Two events are observed, in agreement with the background-only prediction of 2.3 ± 0.4 . The current statistics do not allow a conclusive test of the LSND anomaly yet, however this result is based on the data corresponding to approximately 7.2% of the approved protons-on-target (POT) for JSNS². As of the end of 2025 the accumulated POT is roughly half of the planned amount. Further improvements in the selection efficiency and an expansion of the fiducial volume by a factor of a few in total are also anticipated. In addition, the baseline dependence of the anomaly will be investigated using two detectors in the experiment second phase, JSNS²-II [23], with increased POT. This two-detector configuration will

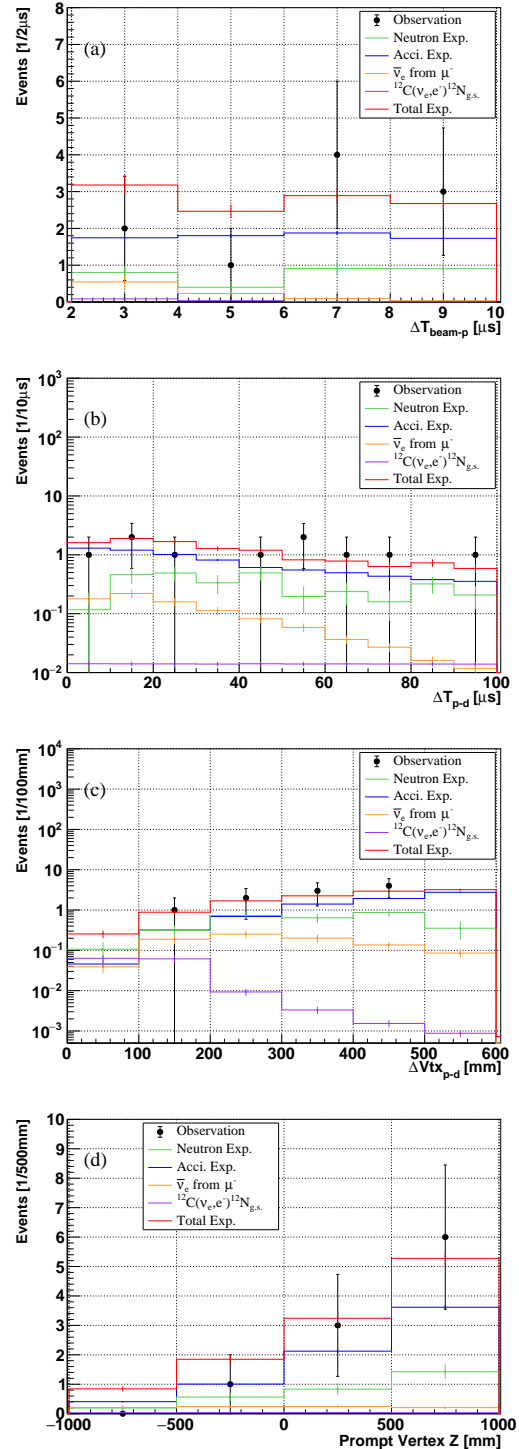


FIG. 5. Distributions of (a) ΔT_{beam-p} , (b) ΔT_{p-d} , (c) ΔVTX_{p-d} and (d) z vertex (height direction) after the PSD application. The vertical axes indicate number of events.

reduce uncertainties in the expected signal rate by enabling a relative measurement as a function of baseline.

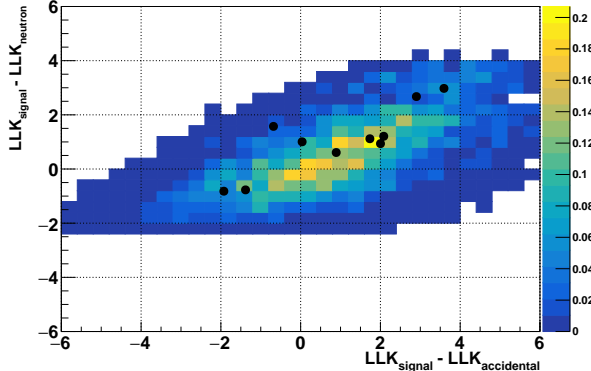


FIG. 6. Two-dimensional log-likelihood ratio distribution for the observation (black points) and the expected background distribution, consisting of backgrounds, shown with the predicted number of events in main text.

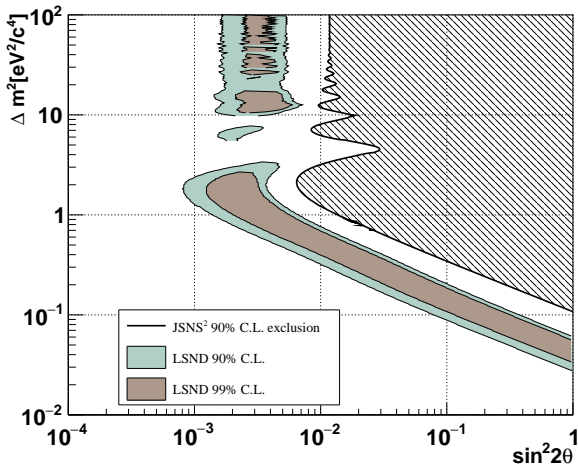


FIG. 7. 90% C.L. exclusion limit derived from the observation (black line). Shaded region shows the excluded region of the neutrino oscillation model.

ACKNOWLEDGMENTS

We deeply thank the J-PARC for their continuous support, especially for the MLF and the accelerator groups to provide an excellent environment for this experiment. We acknowledge the support of the Ministry of Education, Culture, Sports, Science, and Technology (MEXT) and the JSPS grants-in-aid: No. 16H06344, No. 16H03967, No. 23K13133, No. 24K17074, No. 20H05624 and No. 25H00649, Japan. This work is also supported by the National Research Foundation of Korea (NRF): No. 2016R1A5A1004684, No. RS-2016-NR018633, No. 17K1A3A7A09015973, No. 017K1A3A7A09016426, No. 2019R1A2C3004955, No. 2016R1D1A3B02010606, No. 017R1A2B4011200, No. 2018R1D1A1B07050425, No. 2020K1A3A7A09080133, No. 020K1A3A7A09080114, No. 2020R1I1A3066835, No. 2021R1A2C1013661, No. NRF-2021R1C1C2003615, No. 2021R1A6A1A03043957, No. 2022R1A5A1030700, No. RS-2022-NR070836 No. RS-2023-00212787, No. 2023R1A2C1006091, No. RS-2024-00416839, No. RS-2024-00442775 and No. RS-2024-00416839. Our work has also been supported by a fund from the BK21 of the NRF. The University of Michigan gratefully acknowledges the support of the Heising-Simons Foundation. This work conducted at Brookhaven National Laboratory was supported by the U.S. Department of Energy under Contract DE-AC02-98CH10886. The work of the University of Sussex is supported by the Royal Society grant No. IESnR3n170385. We also thank the Daya Bay Collaboration for providing the Gd-LS, the RENO collaboration for providing the LS and PMTs, CIEMAT for providing the splitters, Drexel University for providing the FEE circuits and Tokyo Inst. Tech for providing FADC boards.

DATA AVAILABILITY

The data that support the findings of this article are not publicly available. The data are available from the authors upon reasonable request.

[1] M. Harada *et al.* (JSNS² Collaboration), Proposal: A Search for Sterile Neutrino at J-PARC Materials and Life Science Experimental Facility, arXiv:1310.1437.

[2] S. Ajimura *et al.* (JSNS² Collaboration), Technical Design Report (TDR): Searching for a Sterile Neutrino at J-PARC MLF (E56, JSNS²), (2017), arXiv:1705.08629.

[3] C. Athanassopoulos *et al.* (LSND Collaboration), Evidence for $\bar{\nu}_\mu \rightarrow \bar{\nu}_e$ Oscillations from the LSND Experiment at the Los Alamos Meson Physics Facility, Phys. Rev. Lett. **77**, 3082 (1996).

[4] V. V. Barinov *et al.* (BEST Collaboration), Search for electron-neutrino transitions to sterile states in the BEST experiment, Phys. Rev. C **105**, 065502 (2022).

[5] A. A. A. Arevalo *et al.* (MiniBooNE Collaboration), Significant Excess of ElectronLike Events in the MiniBooNE Short-Baseline Neutrino Experiment, Phys. Rev. Lett. **121**, 221801 (2018).

[6] G. Mention, M. Fechner, T. Lasserre, T. A. Mueller, D. Lhuillier, M. Cribier, and A. Letourneau, The reactor antineutrino anomaly, Phys. Rev. D **83**, 073006 (2011).

- [7] S. Ajimura *et al.* (JSNS² Collaboration), The JSNS² detector, Nucl. Instrum. Methods Phys. Res., Sect. A **1014**, 165742 (2021).
- [8] T. Dodo *et al.* (JSNS² Collaboration), The first JSNS2 measurement of electron neutrino flux using $^{12}\text{C}(\nu_e, e^-)$ $^{12}\text{N}_{g.s.}$ reaction, Phys. Rev. D **112**, 032012 (2025).
- [9] B. Armbruster *et al.* (KARMEN Collaboration), Upper limits for neutrino oscillations $\bar{\nu}_\mu \rightarrow \bar{\nu}_e$ from muon decay at rest, Phys. Rev. D **65**, 112001 (2002).
- [10] Y. Hino *et al.* (JSNS² Collaboration), Characterization of the correlated background for a sterile neutrino search using the first dataset of the JSNS² experiment, Eur. Phys. J. C **82**, 331 (2022).
- [11] T. Dodo *et al.* (JSNS² Collaboration), Pulse Shape Discrimination in JSNS², Prog. Theo. Exp. Phys. **2025**, 023H02 (2025).
- [12] Y. Hino *et al.* (JSNS² Collaboration), Stainless steel tank production and tests for the JSNS² neutrino detector, J. Instrum. **14**, T09010 (2019).
- [13] Eljen, Eljen's Safety Data Sheet, 10.7302/6288.
- [14] J. S. Park *et al.*, The JSNS² data acquisition system, J. Instrum. **15**, T09002 (2020).
- [15] J. Jordan, *Physics at short baseline neutrino experiments*, Ph.D. thesis, University of Michigan (2022).
- [16] D. H. Lee *et al.*, Evaluation of the performance of the event reconstruction algorithms in the JSNS2 experiment using a 252Cf calibration source, arXiv:2404.04153.
- [17] E. Marzec *et al.*, First Measurement of Missing Energy Due to Nuclear Effects in Monoenergetic Neutrino Charged Current Interactions, Phys. Rev. Lett. **134**, 081801 (2025).
- [18] D. H. Lee *et al.*, Muon tagging with Flash ADC waveform baselines, J. Instrum. **20**, P09002.
- [19] F. An *et al.* (Daya-Bay Collaboration), Observation of Electron-Antineutrino Disappearance at Daya Bay, Phys. Rev. Lett. **108**, 171803 (2012).
- [20] D. H. Lee *et al.* (JSNS² Collaboration), Study on the accidental background of the JSNS² experiment, Eur. Phys. J. C **89**, 409 (2024).
- [21] P. Vogel and J. F. Beacom, The angular distribution of the reaction $\bar{\nu}_e + p \rightarrow e^+ + n$, Phys. Rev. D **60**, 053003 (1999).
- [22] G. J. Feldman and R. D. Cousins, Unified approach to the classical statistical analysis of small signals, Phys. Rev. D **57**, 3873–3889 (1998).
- [23] S. Ajimura *et al.* (JSNS²-II Collaboration), Proposal: JSNS²-II, arXiv:2012.10807.